

# Weighted Guided Image Filtering

Zhengguo Li, *Senior Member, IEEE*, Jinghong Zheng, *Member, IEEE*, Zijian Zhu, *Member, IEEE*,  
Wei Yao, *Member, IEEE*, and Shiqian Wu, *Senior Member, IEEE*

**Abstract**—It is known that local filtering-based edge-preserving smoothing techniques suffer from halo artifacts. In this paper, a weighted guided image filter (WGIF) is introduced by incorporating an edge-aware weighting into an existing guided image filter (GIF) to address the problem. The WGIF inherits advantages of both global and local smoothing filters in the sense that: 1) the complexity of the WGIF is  $O(N)$  for an image with  $N$  pixels, which is same as the GIF and 2) the WGIF can avoid halo artifacts like the existing global smoothing filters. The WGIF is applied for single image detail enhancement, single image haze removal, and fusion of differently exposed images. Experimental results show that the resultant algorithms produce images with better visual quality and at the same time halo artifacts can be reduced/avoided from appearing in the final images with negligible increment on running times.

**Index Terms**—Edge-preserving smoothing, weighted guided image filter, edge-aware weighting, detail enhancement, haze removal, exposure fusion.

## I. INTRODUCTION

MANY applications in the fields of computational photography and image processing require smoothing techniques that can preserve edge well. Typical examples include image de-noising [1], [2], fusion of differently exposed images [3], tone mapping of high dynamic range (HDR) images [4], detail enhancement via multi-lighting images [5], texture transfer from a source image to a destination image [6], single image haze removal [7], and etc. The smoothing process usually decomposes an image to be filtered into two layers: a base layer formed by homogeneous regions with sharp edges and a detail layer which can be either noise, e.g., a random pattern with zero mean, or texture, such as a repeated pattern with regular structure.

There are two types of edge-preserving image smoothing techniques. One type is global optimization based filters as in [1], [2], [4], and [8]. The optimized performance criterion consists of a data term and a regularization term. The data

Manuscript received April 28, 2014; revised September 8, 2014 and October 20, 2014; accepted November 10, 2014. Date of publication November 14, 2014; date of current version December 8, 2014. The associate editor coordinating the review of this manuscript and approving it for publication was Dr. Xin Li.

Z. Li, J. Zheng, Z. Zhu, and W. Yao are with the Department of Signal Processing, Institute for Infocomm Research, Singapore 138632 (e-mail: ezgli@i2r.a-star.edu.sg; jzheng@i2r.a-star.edu.sg; zhuzj@i2r.a-star.edu.sg; wyao@i2r.a-star.edu.sg).

S. Wu is with the College of Machinery and Automation, Wuhan University of Science and Technology, Wuhan 430081, China (e-mail: shiqian.wu@wust.edu.cn).

Color versions of one or more of the figures in this paper are available online at <http://ieeexplore.ieee.org>.

Digital Object Identifier 10.1109/TIP.2014.2371234

term measures fidelity of reconstructed image with respect to the image to be filtered while the regularization term provides the smoothness level of the reconstructed image. Even though the global optimization based filters often yield excellent quality, they have high computational cost. The other type is local filters such as bilateral filter (BF) [9], its extension in gradient domain [10], trilateral filter [11], and their accelerated versions [5], [12], [13] as well as guided image filter (GIF) [14]. Compared with the global optimization based filters, the local filters are generally simpler. However, the local filters cannot preserve sharp edges like the global optimization based filters [4], [14]. As such, halo artifacts are usually produced by the local filters when they are adopted to smooth edges [14]. It was mentioned in [14] that the local filters such as the BF/GIF would concentrate the blurring near these edges and introduce halos while the global optimization based filters such as the weighted least squares (WLS) filter in [4] would distribute such blurring globally. It is worth noting that the Lagrangian factor in the WLS filter [4] is content adaptive whether the Lagrangian factor in the GIF and both spatial similarity parameter and range similarity parameter in the BF [9] are fixed. This could be another major reason that the BF/GIF produces halo artifacts. It is worth noting that the reason was also noticed in [15] and [16]. The range similarity parameter of the BF in [15] is adaptive to the content of the image to be filtered while both the spatial similarity and the range similarity parameters of the BF in [16] are adaptive to the content of the image to be filtered. Unfortunately, as pointed out in [15], adaptation of the parameters will destroy the 3D convolution form, and the adaptive BF (ABF) cannot be accelerated via the approach in [13]. It is thus desired to design a new local filter which is as fast as the GIF in [14] and preserves edges as well as the WLS filter in [4].

In this paper, an edge-aware weighting is introduced and incorporated into the GIF [14] to form a weighted GIF (WGIF). In human visual perception, edges provide an effective and expressive stimulation that is vital for neural interpretation of a scene [17]. Larger weights are thus assigned to pixels at edges than pixels in flat areas. There are many methods to compute the edge-aware weighting. Local variance in  $3 \times 3$  window of a pixel in a guidance image is applied to compute the edge-aware weighting. The weighting can be easily computed via the box filter in [14] for all pixels in the guidance image. The local variance of a pixel is normalized by the local variances of all pixels in the guidance image. The normalized weighting is then adopted to design the WGIF. Due to the proposed weighting, the WGIF can preserve sharp edges like the global filters [1], [2], [4], [8].

As a result, halo artifacts can be reduced/avoided by using the WGIF. Similar to the GIF in [14], the WGIF also avoids gradient reversal. In addition, the complexity of the WGIF is  $O(N)$  for an image with  $N$  pixels which is the same as that of the GIF in [14]. These features allow many applications of the WGIF in the fields of computational photography and image processing. The WGIF is applied for single image detail enhancement, single image haze removal, and fusion of differently exposed images. Experimental results of the three applications show that the resultant algorithms produce images with excellent visual quality as those of global optimization based algorithms, and at the same time the running times of the proposed algorithms are comparable to the GIF based algorithms. It is worth noting that an adaptive GIF (AGIF) was proposed in [18] for image sharpening and de-noising by borrowing a shifting technique in [15]. It was shown in [18] that the complexity of the AGIF in [18] is  $O(N)$  for an image with  $N$  pixels. On the other hand, both the ABF in [15] and the AGIF in [18] are training-based approaches while no training is required by the WGIF.

The rest of this paper is organized as follows. Existing edge-preserving smoothing techniques are summarized in Section II. Section III includes details on the WGIF. Three applications of the WGIF are given in Section IV. Concluding remarks are provided in Section V.

## II. RELATED WORKS ON EDGE-PRESERVING SMOOTHING TECHNIQUES

In this section, existing edge-preserving smoothing techniques are summarized with the emphasis on the GIF in [14] and the WLS filter in [4].

The task of edge-preserving smoothing is to decompose an image  $X$  into two parts as follows:

$$X(p) = \hat{Z}(p) + e(p), \quad (1)$$

where  $\hat{Z}$  is a reconstructed image formed by homogeneous regions with sharp edges,  $e$  is noise or texture, and  $p (= (x, y))$  is a position.  $\hat{Z}$  and  $e$  are called base layer and detail layer, respectively.

One type of edge-preserving smoothing techniques is based on local filtering. The BF is widely used due to its simplicity [9], [19], [20]. However, the BF could suffer from “gradient reversal” artifacts despite its popularity [14], and the results may exhibit undesired profiles around edges, usually observed in detail enhancement of conventional LDR images or tone mapping of HDR images. The GIF was introduced in [14] to overcome this problem. In the GIF, a guidance image  $G$  is used which could be identical to the image  $X$  to be filtered. It is assumed that  $\hat{Z}$  is a linear transform of  $G$  in the window  $\Omega_{\zeta_1}(p')$  [21]–[23]:

$$\hat{Z}(p) = a_{p'} G(p) + b_{p'}, \quad \forall p \in \Omega_{\zeta_1}(p'), \quad (2)$$

where  $\Omega_{\zeta_1}(p')$  is a square window centered at the pixel  $p'$  of a radius  $\zeta_1$ .  $a_{p'}$  and  $b_{p'}$  are two constants in the window  $\Omega_{\zeta_1}(p')$ .

To determine the linear coefficients  $(a_{p'}, b_{p'})$ , a constraint is added to  $X$  and  $\hat{Z}$  as in Equation (1). The values of  $a_{p'}$  and  $b_{p'}$



Fig. 1. Two tone mapped images. (a)  $\lambda = 2$ ,  $\gamma = 1.2$ , and  $\epsilon = 0.0001$  as in [4]; and (b)  $\lambda = 2$ ,  $\gamma = 0$ , and  $\epsilon = 0$ .

are then obtained by minimizing a cost function  $E(a_{p'}, b_{p'})$  which is defined as

$$E = \sum_{p \in \Omega_{\zeta_1}(p')} [(a_{p'} G(p) + b_{p'} - X(p))^2 + \lambda a_{p'}^2], \quad (3)$$

where  $\lambda$  is a regularization parameter penalizing large  $a_{p'}$ .

Besides the above local filtering based edge-preserving smoothing techniques, another type of edge-preserving smoothing techniques is based on global optimization. The WLS filter in [4] is a typical example and it is derived by minimizing the following quadratic cost function:

$$E = \sum_{p=1}^N [(\hat{Z}(p) - X(p))^2 + \lambda(p) \|\nabla \hat{Z}(p)\|^2], \quad (4)$$

where  $N$  is the total number of pixels in an image,  $\nabla \hat{Z}(p) = [\frac{\partial \hat{Z}(p)}{\partial x}, \frac{\partial \hat{Z}(p)}{\partial y}]^T$ , and  $\lambda(p) = [\lambda_x(p), \lambda_y(p)]^T$  is defined as

$$\lambda_x(p) = \frac{\lambda}{|\frac{\partial X(p)}{\partial x}|^\gamma + \epsilon}; \quad \lambda_y(p) = \frac{\lambda}{|\frac{\partial X(p)}{\partial y}|^\gamma + \epsilon},$$

$\lambda$ ,  $\gamma$  and  $\epsilon$  are three constants. The values of  $\lambda$ ,  $\gamma$  and  $\epsilon$  in [4] are 2, 1.2 and  $10^{-4}$ , respectively.

It is shown in the linear model (2) that  $\nabla \hat{Z}(p) = a_{p'} \nabla G(p)$ . Clearly, the smoothness of  $\hat{Z}$  in  $\Omega_{\zeta_1}(p')$  depends on the value of  $a_{p'}$ . This implies that the data term and the regularization terms in the GIF are similar to those in the WLS filter in the sense that the data term measures the fidelity of  $\hat{Z}$  with respect to the filtered image  $X$  and the regularization term provides the smoothness level of  $\hat{Z}$ . There are two major differences between the WLS filter and the GIF. 1) The GIF in [14] is based on local optimization while the WLS filter in [4] on global optimization. As such, the complexity of the GIF is  $O(N)$  for an image with  $N$  number of pixels and the WLS filter is more complicated than the GIF. 2) The value of  $\lambda$  is fixed in the GIF while it is adaptive to local gradients in the WLS filter. One possible problem for the GIF is halos which can be avoided by the WLS filter. As indicated in [14], the GIF would concentrate blurring near edges and introduce halos while the WLS filter would distribute the blurring globally.

Here, we would argue that the latter is another possibly major reason that halo artifacts can be avoided by the WLS filter. To support our argument, the WLS filter is applied to design a tone mapping algorithm for HDR images. Two tone mapped images are shown in Fig. 1. With the values of  $\lambda$ ,  $\gamma$  and  $\epsilon$  in [4], halo artifacts are avoided from appearing in the final



Fig. 2. (a) An input image, and (b) its weighting.

tone mapped image. However, halo artifacts appear in the final image when the values of  $\lambda_x(p)$  and  $\lambda_y(p)$  are fixed as  $\lambda$ 's. This implies that the spatially varying image gradients aware weighting  $\lambda_x(p)$  and  $\lambda_y(p)$  are crucial for the WLS filter in [4] to avoid halo artifacts.

Unfortunately, the value of  $\lambda$  in the GIF [14] is fixed rather than being spatially varying as in [4]. As such, halos are unavoidable for the GIF in [14] when it is forced to smooth edges.

### III. WEIGHTED GUIDED IMAGE FILTER

In this section, an edge-aware weighting is first proposed and it is incorporated into the GIF in [14] to form the WGIF.

#### A. An Edge-Aware Weighting

Let  $G$  be a guidance image and  $\sigma_{G,1}^2(p')$  be the variance of  $G$  in the  $3 \times 3$  window,  $\Omega_1(p')$ . An edge-aware weighting  $\Gamma_G(p')$  is defined by using local variances of  $3 \times 3$  windows of all pixels as follows:

$$\Gamma_G(p') = \frac{1}{N} \sum_{p=1}^N \frac{\sigma_{G,1}^2(p') + \varepsilon}{\sigma_{G,1}^2(p) + \varepsilon}, \quad (5)$$

where  $\varepsilon$  is a small constant and its value is selected as  $(0.001 \times L)^2$  while  $L$  is the dynamic range of the input image. All pixels in the guidance image are used in the computation of  $\Gamma_G(p')$ . In addition, the weighting  $\Gamma_G(p')$  measures the importance of pixel  $p'$  with respect to the whole guidance image. Due to the box filter in [14], the complexity of  $\Gamma_G(p')$  is  $O(N)$  for an image with  $N$  pixels.

The value of  $\Gamma_G(p')$  is usually larger than 1 if  $p'$  is at an edge and smaller than 1 if  $p'$  is in a smooth area. Clearly, larger weights are assigned to pixels at edges than those pixels in flat areas by using the weight  $\Gamma_G(p')$  in Equation (5). Applying this edge-aware weighting, there might be blocking artifacts in final images. To prevent possible blocking artifacts from appearing in the final image, the value of  $\Gamma_G(p')$  is smoothed by a Gaussian filter. The smoothed weights of all pixels in Fig. 2(a) are shown in Fig. 2(b). Clearly, larger weights are assigned to pixels at edges than those pixels in flat areas. The proposed weighting matches one feature of human visual system, i.e., pixels at sharp edges are usually more important than those in flat areas [17].

It should be pointed out that the proposed weighting  $\Gamma_G(p')$  is one edge-aware weighting, and there are many other edge-aware weighting including those derived by the

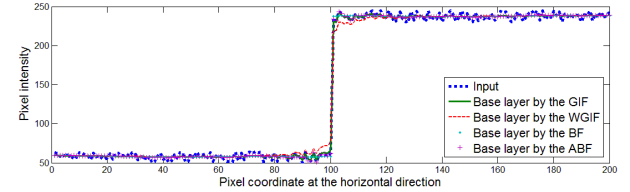


Fig. 3. 1-D illustration of the WGIF, the GIFT in [14], the BF in [9], and the ABF in [16]. The values of  $\zeta_1$  and  $\lambda$  in both the WGIF and the GIFT are 15 and  $1/64$ , respectively. The values of  $\sigma_1$  and  $\sigma_2$  in both the BF and the ABF are 15 and 0.2, respectively.

Sobel gradient and the Roberts gradient [24]. The GIFT can be improved by incorporating these edge-aware weighting into the GIFT. In the following section, the proposed weighting  $\Gamma_G(p')$  in Equation (5) is used as an example to illustrate the WGIF.

#### B. The Proposed Filter

Same as the GIFT, the key assumption of the WGIF is a local linear model between the guidance image  $G$  and the filtering output  $\hat{Z}$  as in Equation (2). The model ensures that the output  $\hat{Z}$  has an edge only if the guidance image  $G$  has an edge.

The proposed weighting  $\Gamma_G(p')$  in Equation (5) is incorporated into the cost function  $E(a_{p'}, b_{p'})$  in Equation (3). As such, the solution is obtained by minimizing the difference between the image to be filtered  $X$  and the filtering output  $\hat{Z}$  while maintaining the linear model (2), i.e., by minimizing a cost function  $E(a_{p'}, b_{p'})$  which is defined as

$$E = \sum_{p \in \Omega_{\zeta_1}(p')} [(a_{p'} G(p) + b_{p'} - X(p))^2 + \frac{\lambda}{\Gamma_G(p')} a_{p'}^2]. \quad (6)$$

The optimal values of  $a_{p'}$  and  $b_{p'}$  are computed as

$$a_{p'} = \frac{\mu_{G \odot X, \zeta_1}(p') - \mu_{G, \zeta_1}(p') \mu_{X, \zeta_1}(p')}{\sigma_{G, \zeta_1}^2(p') + \frac{\lambda}{\Gamma_G(p')}}, \quad (7)$$

$$b_{p'} = \mu_{X, \zeta_1}(p') - a_{p'} \mu_{G, \zeta_1}(p'), \quad (8)$$

where  $\odot$  is the element-by-element product of two matrices.  $\mu_{G \odot X, \zeta_1}(p')$ ,  $\mu_{G, \zeta_1}(p')$  and  $\mu_{X, \zeta_1}(p')$  are the mean values of  $G \odot X$ ,  $G$  and  $X$ , respectively.

The final value of  $\hat{Z}(p)$  is given as follows:

$$\hat{Z}(p) = \bar{a}_{p'} G(p) + \bar{b}_{p'}, \quad (9)$$

where  $\bar{a}_{p'}$  and  $\bar{b}_{p'}$  are the mean values of  $a_{p'}$  and  $b_{p'}$  in the window computed as

$$\bar{a}_{p'} = \frac{1}{|\Omega_{\zeta_1}(p)|} \sum_{p' \in \Omega_{\zeta_1}(p)} a_{p'}; \quad \bar{b}_{p'} = \frac{1}{|\Omega_{\zeta_1}(p)|} \sum_{p' \in \Omega_{\zeta_1}(p)} b_{p'}, \quad (10)$$

and  $|\Omega_{\zeta_1}(p')|$  is the cardinality of  $\Omega_{\zeta_1}(p')$ .

For easy analysis, the images  $X$  and  $G$  are assumed to be the same. Consider the case that the pixel  $p'$  is at an edge. The value of  $\Gamma_X(p')$  is usually much larger than 1.  $a_{p'}$  in the WGIF is closer to 1 than  $a_{p'}$  in the GIFT [14]. This implies that sharp edges are preserved better by the WGIF than the GIFT. As shown in Fig. 3, edges are indeed preserved much better

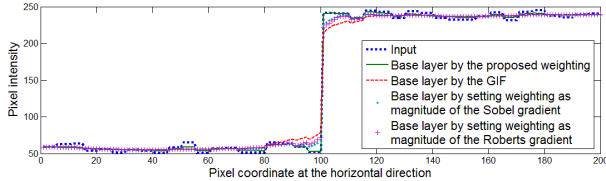


Fig. 4. 1-D illustration of three different WGIFs and the GIF in [14]. The values of  $\zeta_1$  and  $\lambda$  are 15 and 1/32, respectively.

by the WGIF. In addition, the complexity of the WGIF is  $O(N)$  for an image with  $N$  pixels which is the same as that of the GIF. Edges are also preserved well by the ABF in [16] while the complexity of the ABF is an issue.

#### IV. APPLICATIONS OF THE WGIF

In this section, the WGIF is adopted to study single image detail enhancement, single image haze removal, and fusion of differently exposed images. All algorithms are implemented by using the MATLAB 2008b, and all the simulations were carried on Dell Precision T7400 with Intel Quad Core CPU 3.2 GHz and 4GB of RAM. Readers are invited to view the electronic version of the full-size figures in order to better appreciate the differences among images.

##### A. Single Image Detail Enhancement

We first consider the case that the whole image is enhanced and it is called “full detail enhancement”. With the WGIF, the input image  $X$  is decomposed into  $\hat{Z}$  and  $e$  as shown in Equation (1) and the details enhancement can be achieved as follows:

$$Z_{enh}(p) = X(p) + \theta e(p), \quad (11)$$

where  $\theta (> 0)$  is a positive constant and is called an amplification factor. Its value is fixed as 4 in our experimental results according to the recommendation in [14] provided that it is specified.

Since this paper focuses on introducing an edge-aware weighting to the GIF [14], three different methods on the computation of edge-aware weighting are first compared, and one is the proposed weighting in Equation (5) and the other two are

$$\hat{\Gamma}_G(p') = \sqrt{\left(\frac{\partial Z(p')}{\partial x}\right)_s^2 + \left(\frac{\partial Z(p')}{\partial y}\right)_s^2}, \quad (12)$$

$$\check{\Gamma}_G(p') = \sqrt{\left(\frac{\partial Z(p')}{\partial x}\right)_r^2 + \left(\frac{\partial Z(p')}{\partial y}\right)_r^2}. \quad (13)$$

$\hat{\Gamma}_G(p')$  is the magnitude of the Sobel gradient, and  $\check{\Gamma}_G(p')$  is the magnitude of the Roberts gradient [24]. Similar to Fig. 3, a simple 1-D example is tested. It is illustrated in Fig. 4 that the proposed weighting preserves edges slightly better than both  $\hat{\Gamma}_G(p')$  and  $\check{\Gamma}_G(p')$ .

Besides comparing three different methods on the computation of weighting, the WGIF is compared with the GIF in [14] by choosing three different values of  $\theta$  as 1, 4 and 9. The quality metric in [25] is used to evaluate enhanced images.

The scores of the six images in Fig. 5 are 37.84, 40.98, 38.37, 55.97, 35.89, and 57.89, respectively. With the metric, a higher value represents a higher quality. It is also shown in Fig. 5 that the GIF in [14] is more sensitive to the value of  $\theta$  in terms of halo artifacts. The halo artifacts by the GIF in [14] as well as the amplified noise by both the GIF in [14] and the WGIF become more visible when the value of  $\theta$  is enlarged. This implies that the value of  $\theta$  also plays an important role in the generation of halo artifacts and the amplification of noise. The observation will serve as a guideline for the design of single image haze removal algorithm in Section IV-B.

Two images are also tested to compare the WGIF with the BF in [9], the GIF in [14] and the  $l_0$  norm based global optimization algorithm in [8]. The values of  $\sigma_1$  and  $\sigma_2$  are 16 and 0.1 for the BF in [9]. The values of  $\lambda$  and  $\zeta_1$  are respectively selected as 1/128 and 16 for both the WGIF and the GIF in [14].  $\kappa$  and  $\lambda$  in [8] are respectively set as 2 and 0.02 as in the MATLAB code provided by the authors. As indicated by the red arrows in Fig. 6, the WGIF can be used to produce enhanced images with better visual quality. In addition, halo artifacts are avoided via the WGIF while there are halo artifacts in output images by the GIF in [14] and the BF in [9], and gradient reversal artifacts by the global optimization based algorithm in [8]. The quality metric in [25] is also used to evaluate the enhanced images. As shown in Table 1, the objective quality is also improved by the WGIF.

The proposed detail enhancement algorithm in Equation (11) and the existing ones in [8] and [14] amplify all fine details of an input image to obtain an image with more fine details. However, there is a fundamental limitation for full detail enhancement algorithms, i.e., noise is also amplified when fine details are enhanced. The human visual system can tolerate amplified noise in complex regions but is particularly sensitive to amplified noise in flat areas. Separating the noise from fine details is also known to be very challenging. To overcome the limitation of full detail enhancement algorithms, a selective detail enhancement algorithm is introduced as follows:

$$Z_{enh}(p) = X(p) + \eta(p)\theta e(p), \quad (14)$$

where the value of  $\eta(p)$  is computed by using  $\Gamma_G(p)$  in Equation (5). Its value is almost 0 if the pixel  $p$  is in a flat region and 1 otherwise.

With the proposed selective detail enhancement algorithm, fine details in all areas except flat ones are enhanced. The visual quality of the final enhanced image can be improved. To illustrate this, three different detail enhancement algorithms are compared, and they are 1) a full detail enhancement algorithm based on the guided filter in [14], 2) the proposed full detail enhancement algorithm in Equation (11), and 3) a selective detail enhancement algorithm in Equation (14). As shown by the zoomed-in regions in Fig. 7, noise in flat regions is amplified by using both full detail enhancement algorithms while this problem is overcome by using the selective detail enhancement algorithm in Equation (14). Therefore, the visual quality of final images is improved by using the proposed selective detail enhancement algorithm.



Fig. 5. Comparison of the WGIF with the GIF in [14] by choosing four different values of  $\theta$ . The values of  $\zeta_1$  and  $\lambda$  are 15 and 1/128, respectively. (a, c, e) by the GIF in [14] with the value of  $\theta$  as 1, 4, and 9, respectively. (b, d, f) by the WGIF with the value of  $\theta$  as 1, 4, and 9, respectively.



Fig. 6. Comparison of enhanced images via different filters. (a, f) images to be enhanced, (b, g) enhanced image by the BF in [9], (c, h) enhanced images by the GIF in [14], (d, i) enhanced images by the global filter in [8], (e, j) enhanced images by the WGIF.

TABLE I  
OBJECTIVE EVALUATION ON THE ENHANCED IMAGES IN FIG. 6

| Image  | 1     | 2     | 3     | 4     | 5     |
|--------|-------|-------|-------|-------|-------|
| Top    | 27.22 | 27.34 | 27.81 | 28.52 | 37.7  |
| Bottom | 36.87 | 48.57 | 33.04 | 41.72 | 35.91 |

### B. Single Image Haze Removal

Images of outdoor scenes could be degraded by haze, fog, and smoke in the atmosphere. The degraded images lose the contrast and color fidelity. Haze removal is thus highly desired in both computational photography and computer vision applications. The model adopted to describe the formulation of a haze image is given as [26]

$$X_c(p) = \hat{Z}_c(p)t(p) + A_c(1 - t(p)), \quad (15)$$

where  $c \in \{r, g, b\}$  is a color channel index,  $X_c$  is the observed intensity,  $\hat{Z}_c$  is the scene radiance,  $A_c$  is the global atmospheric light, and  $t$  is the medium transmission describing the portion of the light that is not scattered and reaches the camera.

The first term  $\hat{Z}_c(p)t(p)$  is called direct attenuation [27] and it describes the scene radiance and its decay in the medium. The second term  $A_c(1 - t(p))$  is called airlight. Airlight results from previous scattered light and leads to the shift

of the scene color. When the atmosphere is homogenous, the transmission  $t(p)$  can be expressed as:

$$t(p) = e^{-\alpha d(p)}, \quad (16)$$

where  $\alpha$  is the scattering coefficient of the atmosphere. It indicates that the scene radiance is attenuated exponentially with the scene depth  $d(p)$ . The value of  $\alpha$  is a monotonically increasing function of the haze degree. When the haze becomes heavier, the term  $A_c(1 - t(p))$  dominates the combination. As a result, the hazed image is smoother and the color fidelity of the hazed image is lost more. The objective of haze removal is to restore  $\hat{Z}$  from the input  $X$ . Halo artifacts, amplification of noise in sky regions, and color fidelity are three major problems to be addressed for single image haze removal [28], [29].

Let  $\Phi_c(\cdot)$  be a minimal operation along the color channel  $\{r, g, b\}$  and it is defined as

$$A_{min} = \Phi_c(A_c) = \min\{A_r, A_g, A_b\}, \quad (17)$$

$$X_{min}(p) = \Phi_c(X_c(p)) = \min\{X_r(p), X_g(p), X_b(p)\}, \quad (18)$$

$$\hat{Z}_{min}(p) = \Phi_c(\hat{Z}_c(p)) = \min\{\hat{Z}_r(p), \hat{Z}_g(p), \hat{Z}_b(p)\}, \quad (19)$$

it can be derived from the haze image model in Equation (15) that

$$X_{min}(p) = \hat{Z}_{min}(p)t(p) + A_{min}(1 - t(p)). \quad (20)$$

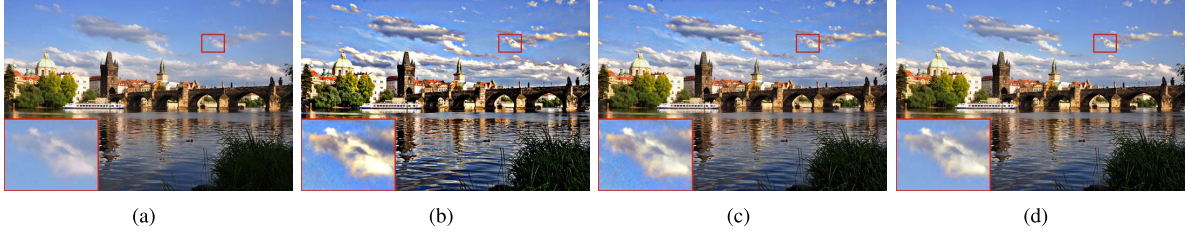


Fig. 7. Comparison of full and selective detail enhancement algorithms. (a) an image to be enhanced, (b) an amplified image by the full detail enhancement algorithm based on the GIF in [14], (c) an amplified image by the full detail enhancement algorithm in Equation (11), (d) an amplified image by the selective detail enhancement algorithm in Equation (14).

Let  $\Psi_{\zeta_2}(\cdot)$  be a minimal operation in the neighborhood  $\Omega_{\zeta_2}(p)$  and it is defined as

$$\Psi_{\zeta_2}(z(p)) = \min_{p' \in \Omega_{\zeta_2}(p)} \{z(p')\}. \quad (21)$$

It is shown in [30] that the complexity of  $\Psi_{\zeta_2}(\cdot)$  is  $O(N)$  for an image with  $N$  pixels. The dark channel in [7] is defined as

$$J_{dark}^{\hat{Z}}(p) = \Phi_c(\Psi_{\zeta_2}(\hat{Z}_c(p))), \quad (22)$$

where the value of  $\zeta_2$  is 7 in [7]. Even though the complexity of  $\Psi_{\zeta_2}(\cdot)$  is  $O(N)$  for an image with  $N$  pixels, three minimal operations  $\Psi_{\zeta_2}(\cdot)$  and one minimal operation  $\Phi_c(\cdot)$  are required to compute  $J_{dark}^{\hat{Z}}(p)$  for the pixel  $p$ . Inspired by the haze image model in Equation (20), a simplified dark channel is defined as

$$\hat{J}_{dark}^{\hat{Z}}(p) = \Psi_{\zeta_2}(\Phi_c(\hat{Z}_c(p))). \quad (23)$$

With the new dark channel  $\hat{J}_{dark}^{\hat{Z}}(p)$ , only one minimal operations  $\Psi_{\zeta_2}(\cdot)$  and one minimal operation  $\Phi_c(\cdot)$  are required to compute the dark channel for the pixel  $p$ . Clearly, the computational cost of  $\hat{J}_{dark}^{\hat{Z}}(p)$  is lower than that of  $J_{dark}^{\hat{Z}}(p)$ .

Similar to [7], the value of  $t(p)$  is assumed to be constant in the neighborhood  $\Omega_{\zeta_2}(p)$ . It can be derived from Equation (20) that

$$\hat{J}_{dark}^X(p) = \hat{J}_{dark}^{\hat{Z}}(p)t(p) + A_{min}(1 - t(p)). \quad (24)$$

Since  $\hat{J}_{dark}^{\hat{Z}}(p) \approx 0$ , the value of  $t(p)$  can be initially estimated as

$$t(p) = 1 - \frac{\hat{J}_{dark}^X(p)}{A_{min}}. \quad (25)$$

It is worth noting that the initial value of  $t(p)$  in [7] is given as

$$t(p) = 1 - \Phi_c(\Psi_{\zeta_2}(\frac{\hat{Z}_c(p)}{A_c})). \quad (26)$$

Obviously, it is simpler to estimate the initial value of  $t(p)$  by using the proposed simplified dark channel.

The value of  $A_c(c \in \{r, g, b\})$  is estimated by using  $\hat{J}_{dark}^X(p)$  and  $X_c(p)$ . The brightest pixels in the dark channel are first selected. The value of  $A_c(c \in \{r, g, b\})$  is set as the average intensity of these pixels along each color channel. The initial value of  $t(p)$  is then computed as

$$t(p) = 1 - \frac{31}{32} \frac{\hat{J}_{dark}^X(p)}{A_{min}}. \quad (27)$$

The estimated transmission map  $t(p)$  is then filtered by using the WGIF (5)–(10) with the guidance image as the luminance component of the haze image. The value of  $\lambda$  is set to 1/1000 as in [14] and [29] and the value of  $\zeta_1$  to 60. The value of the transmission map  $t(p)$  is further adjusted as

$$t(p) = t^{1+\varsigma}(p), \quad (28)$$

where the value of  $\varsigma$  is adaptive to the haze level of the input image. Its value is 0/0.03125/0.0625 if the input image is with light/normal/heavy haze.

Finally, the scene radiance  $\hat{Z}(p)$  is recovered by

$$\hat{Z}_c(p) = \frac{X_c(p) - A_c}{t(p)} + A_c; \quad c \in \{r, g, b\}. \quad (29)$$

Equation (29) is equivalent to

$$\hat{Z}_c(p) = X_c(p) + (\frac{1}{t(p)} - 1)(X_c(p) - A_c). \quad (30)$$

It is shown in Equation (16) that the value of  $t(p)$  is always less than or equal to 1, the single image haze removal thus can be regarded as a type of spatially varying detail enhancement. The detail layer is given as  $(X_c(p) - A_c)$  and the amplification factor is  $(\frac{1}{t(p)} - 1)$  which is spatially varying. Since the color of the sky is usually very similar to the atmospheric light  $A_c$  in a haze image, it can be shown that

$$\frac{\hat{J}_{dark}^X(p)}{A_{min}} \rightarrow 1, \text{ and } \frac{1}{t(p)} - 1 \rightarrow 31. \quad (31)$$

This implies that the value of the amplification factor is very large if the pixel  $p$  belongs to the sky region. A lower bound is predefined for the transmission map  $t(p)$  in [7] and [14] so as to limit the amplification factor. The lower bound is selected as 0.1 in [7] and [14]. Similar to Equation (31), it can be computed that the the value of the amplification factors is about 9 if the pixel  $p$  belongs to the sky region. Experimental results in Fig. 5 show that noise could be amplified and/or halo artifacts could be produced due to the large amplification factors. An intuitive method is to select a large lower bound. Unfortunately, a large lower bound will preserve too much haze in the final image. A non-negative sky region compensation term is introduced to adjust the initial value of the transmission map  $t(p)$  in the sky region according to the haze degree of the input image  $X_c$ . The haze degree can be automatically detected by using the histogram of the image  $X_c$ . With the proposed sky region compensation term, the amplification factors in the sky region are reduced.

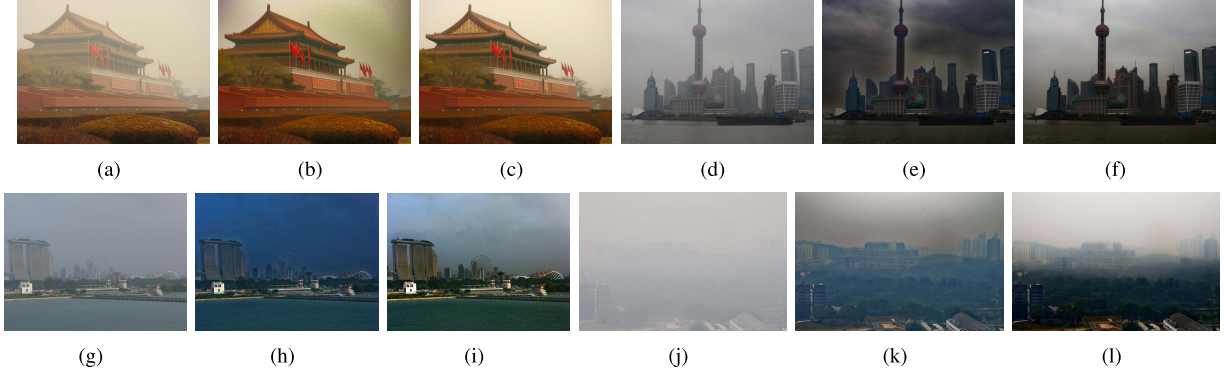


Fig. 8. Comparison of the proposed haze removal algorithm and the haze removal algorithm in [14]. (a, d, g, j) four images with haze; (b, e, h, k) de-hazed images by the algorithm in [14]; (c, f, i, l) de-hazed images by the proposed algorithm.



Fig. 9. Comparison of the proposed haze removal algorithm and the haze removal algorithm in [14] by using two sets of images without haze. (a, d) two images without haze; (b, e) de-hazed images by the algorithm in [14]; (c, f) de-hazed images by the proposed algorithm.

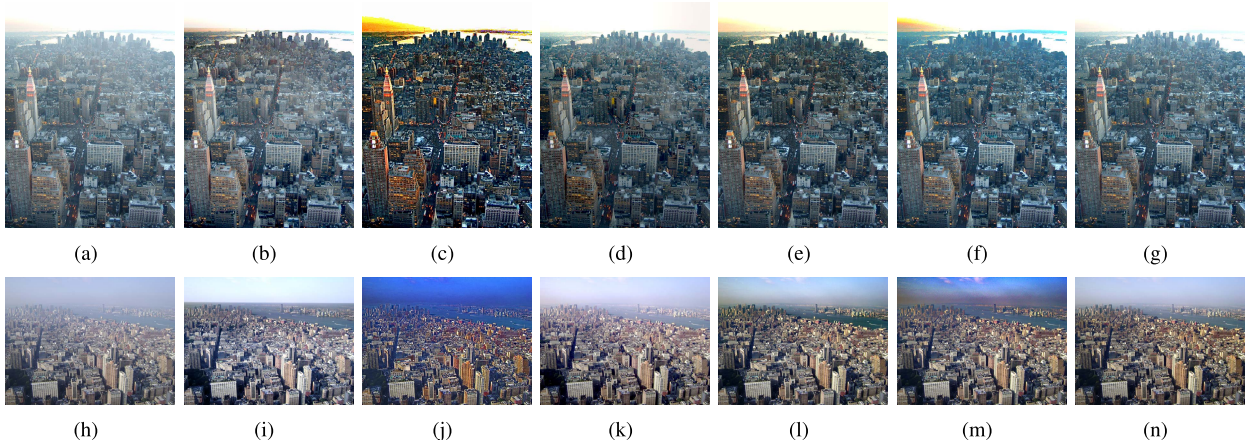


Fig. 10. Haze removal results by the algorithms in [7], [14], [27], [33], and [34] and the proposed algorithm. (a, h) input images; (b, i) de-hazed images by the algorithm in [34]; (c, j) de-hazed images by the algorithm in [27]; (d, k) de-hazed images by the algorithm in [33]; (e, l) de-hazed images by the algorithm in [7]; (f, m) de-hazed images by the algorithm in [14]; and (g, n) de-hazed images by the proposed algorithm.

As such, halo artifacts can be reduced/avoided from appearing in the final image  $\hat{Z}_c$ , and amplification of noise can be limited in the sky region. On the other hand, a very small amount of haze is left for the distant objects. Fortunately, the presence of haze is a fundamental cue for human to perceive depth [31], [32]. Therefore, the left very small amount of haze for the distant objects helps preserve the feeling of depth in the dehazed image better as shown in Figs 8–10.

The proposed algorithm is first compared with the algorithm in [14] by testing four images with haze and two images without haze. As can be seen from Fig. 8, the proposed algorithm neither has artifacts in sky regions nor halo artifacts as opposed to those from [14]. The resolutions of the images in Fig. 8 are  $600 \times 450$ ,  $1600 \times 1200$ ,  $2592 \times 1944$ ,

and  $2144 \times 1424$ , respectively. The running times of the proposed algorithm are respectively 0.8, 5.25, 13.7, and 8.31 seconds while those of the algorithm in [14] are respectively 0.86, 5.32, 13.62, and 8.1 seconds. The speed of the proposed algorithm is comparable to the algorithm in [14]. The two images without haze and their dehazed images are demonstrated in Fig. 9. The proposed algorithm introduces less color distortion than the algorithm in [14]. Clearly, the quality of the dehazed images by the proposed algorithm is much better than the quality of the dehazed images by the haze removal algorithm in [14].

The proposed algorithm is then compared with the algorithms in [7], [14], [27], [33], and [34] by testing two images with haze. As illustrated in Fig. 10, the images

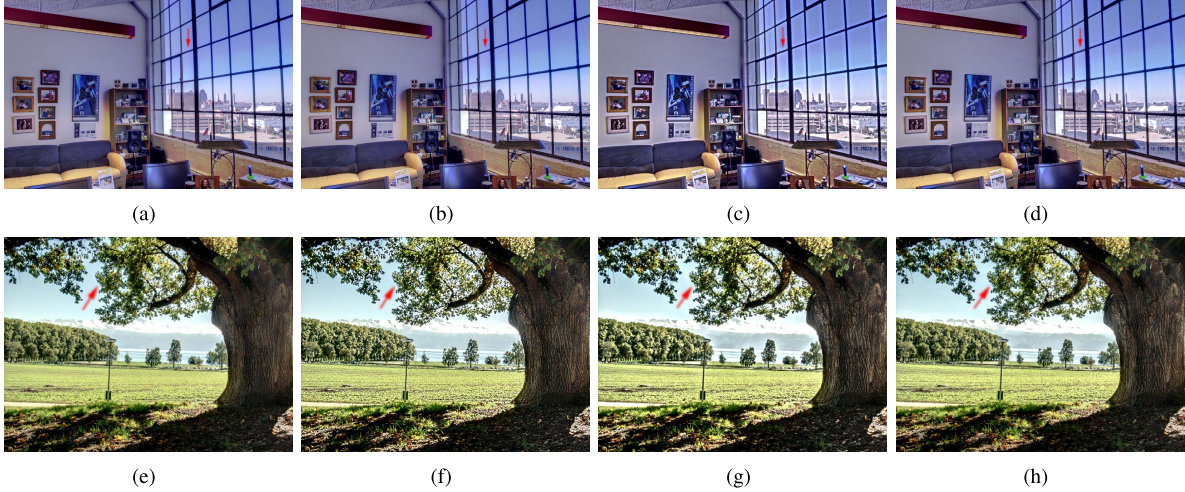


Fig. 11. Comparison of different exposure fusion algorithms. (a, e) images via the exposure fusion algorithm in [35], (b, f) images via the fully detail-enhanced exposure fusion algorithm in [3], (c, g) images via a fully detail-enhanced exposure fusion algorithm based on the GIF in [14], (d, h) images via a fully detail-enhanced exposure fusion algorithm based on the WGIF.

de-hazed by the proposed algorithm are very close to those using the algorithm in [33] and [7]. The colors of the images dehazed by the algorithm in [27] is over saturated. 3D models and texture maps of the scene are required by the algorithm in [34]. The additional information could come from Google Earth or satellite images.

As indicated in [14], one of the key performance improvement in [14] is that the algorithm is much simpler compared to the algorithm in [7]. The running time of the GIF is about 40ms for a  $600 \times 400$  image while 10 seconds using the matting Laplacian matrix as in [7]. Therefore, the proposed de-hazing algorithm has the similar fast speed feature like [14] and it has excellent visual quality of the global optimization based algorithm in [7].

### C. Fusion of Differently Exposed Images

One of the challenges in digital image processing research is the rendering of a HDR natural scene on a conventional LDR display. This challenge can be addressed by capturing multiple LDR images at different exposure levels. Each LDR image only records a small portion of the dynamic range and partial scene details but the whole set of LDR images collectively contain all scene details. All the differently exposed images can be fused together to produce a LDR image by an exposure fusion algorithm [35]. Similar to the detail enhancement of a LDR image, halo artifacts, gradient reversal artifacts and amplification of noise in smooth regions are three major problems to be addressed for the fusion of differently exposed images.

Let input images be denoted as  $X_k (1 \leq k \leq L)$  and their luminance components denoted as  $Y_k (1 \leq k \leq L)$ . The value of  $\Gamma_G(p')$  is computed by using all luminance components  $Y_k (1 \leq k \leq L)$  in log domain. Let  $\sigma_{\log(Y_k),1}^2(p')$  be the local variance of  $\log(Y_k)$  in the  $3 \times 3$  square window centered at the pixel  $p'$ . Due to different exposures, a well exposed pixel in one input image could be under/over-exposed in another image. This implies that the value of  $\sigma_{\log(Y_k),1}^2(p')$  is different

for different  $k$ . On the other hand, gradient magnitude becomes larger when a pixel gets better exposed, and it decreases as the pixel becomes under/over-exposed. The overall local variance at pixel  $p'$  is thus computed as

$$\tilde{\sigma}^2(p') = \frac{\sum_{k=1}^L w_k(p') (\sigma_{\log(Y_k),1}^2(p') + 0.001)}{\sum_{k=1}^L w_k(p')} \quad (32)$$

where  $w_k(p')$  is given as

$w_k(p') = 77\gamma(Z_{k,1}(p')) + 150\gamma(Z_{k,2}(p')) + 29\gamma(Z_{k,3}(p'))$ ,  
and the weighting function  $\gamma(z)$  is defined as follows [3]:

$$\gamma(z) = \begin{cases} z + 1; & \text{if } z \leq 127 \\ 256 - z; & \text{otherwise.} \end{cases} \quad (33)$$

The value of  $\Gamma_G(p')$  is then given as

$$\Gamma_G(p') = \frac{1}{N} \sum_{p=1}^N \frac{\tilde{\sigma}^2(p')}{\tilde{\sigma}^2(p)}. \quad (34)$$

With the weighting function  $\Gamma_G(p')$  in Equation (34), the fine details of the  $k$ th input image,  $L_k^{(d)}$  are extracted from the image  $Y_k$  individually by using the WGIF (5)–(10). All the extracted fine details  $L_k^{(d)}$  are fused by considering the exposedness levels of all image  $Y_k (1 \leq k \leq L)$  to produce the final fine details as

$$L^{(d)}(p) = \frac{\sum_{k=1}^L L_k^{(d)}(p) w_k(p)}{\sum_{k=1}^L w_k(p)}. \quad (35)$$

The final image is produced as

$$X_f(p) = X_{int}(p) e^{\chi L^{(d)}(p)}, \quad (36)$$

where  $e$  is the natural number.  $\chi$  is constant and its value is selected as 1.  $X_{int}$  is an intermediate image that is fused by using the exposure fusion scheme in [35].

Four different exposure fusion algorithms are compared, and they are 1) the exposure fusion algorithm in [35], 2) the fully detail-enhanced exposure fusion algorithm in [3],

3) a fully detail-enhanced exposure fusion algorithm based on the GIF in [14], and 4) a fully detail-enhanced exposure fusion algorithm based on the WGIF. It is worth noting that the detail enhancement algorithm in [3] is a global optimization based approach. The values of  $\lambda$  and  $\zeta_1$  are respectively selected as 1/4 and 16 for both the WGIF and the GIF in [14]. As indicated by the red arrows in Fig. 11, there are visible halo artifacts in the final images by the GIF in [14] while halo artifacts are reduced/avoided by the WGIF. The visual quality of the fused images by the WGIF is comparable to that of the fused images by the global optimization based approach in [3]. Therefore, the WGIF can be applied to design a detail-enhanced fusion algorithm with the fast speed of the GIF based algorithm and at the same time, it has excellent visual quality of the global optimization based algorithm in [3].

## V. CONCLUSION AND DISCUSSION

A weighted guided image filter (WGIF) is proposed in this paper by incorporating an edge-aware weighting into the guided image filter (GIF). The WGIF preserves sharp edges as well as existing global filters, and the complexity of the WGIF is  $O(N)$  for an image with  $N$  pixels which is almost the same as the GIF. Due to the simplicity of the WGIF, it has many applications in the fields of computational photography and image processing. Particularly, it is applied to study single image detail enhancement, single image haze removal, and fusion of differently exposed images. Experimental results show that the resultant algorithms can produce images with excellent visual quality as those of global filters, and at the same time the running times of the proposed algorithms are comparable to the GIF based algorithms.

It should be pointed out that the ABFs in [15] and [16] appear to be similar to the WGIF. Unfortunately, as pointed out in [15], adaptation of the parameters will destroy the 3D convolution form, and the ABFs cannot be accelerated via the approach in [13]. While the WGIF preserves the simplicity of the GIF in [14]. On the other hand, it was shown in [10] and [36] that both the BF and the ABF can be easily extended to gradient domain while it is very challenging to extend the GIF and the WGIF to gradient domain.

It is noting that the WGIF can also be adopted to design a fast local tone mapping algorithm for high dynamic range images, joint upsampling, flash/no-flash de-noising, and etc. In addition, similar idea can be used to improve the anisotropic diffusion in [37], Poisson image editing in [6], etc. All these research problems will be studied in our future research.

## REFERENCES

- [1] P. Charbonnier, L. Blanc-Feraud, G. Aubert, and M. Barlaud, "Deterministic edge-preserving regularization in computed imaging," *IEEE Trans. Image Process.*, vol. 6, no. 2, pp. 298–311, Feb. 1997.
- [2] L. I. Rudin, S. Osher, and E. Fatemi, "Nonlinear total variation based noise removal algorithms," *Phys. D, Nonlinear Phenomena*, vol. 60, nos. 1–4, pp. 259–268, Nov. 1992.
- [3] Z. G. Li, J. H. Zheng, and S. Rahardja, "Detail-enhanced exposure fusion," *IEEE Trans. Image Process.*, vol. 21, no. 11, pp. 4672–4676, Nov. 2012.
- [4] Z. Farbman, R. Fattal, D. Lischinski, and R. Szeliski, "Edge-preserving decompositions for multi-scale tone and detail manipulation," *ACM Trans. Graph.*, vol. 27, no. 3, pp. 249–256, Aug. 2008.
- [5] R. Fattal, M. Agrawala, and S. Rusinkiewicz, "Multiscale shape and detail enhancement from multi-light image collections," *ACM Trans. Graph.*, vol. 26, no. 3, pp. 51:1–51:10, Aug. 2007.
- [6] P. Pérez, M. Gangnet, and A. Blake, "Poisson image editing," *ACM Trans. Graph.*, vol. 22, no. 3, pp. 313–318, Aug. 2003.
- [7] K. He, J. Sun, and X. Tang, "Single image haze removal using dark channel prior," *IEEE Trans. Pattern Anal. Mach. Intell.*, vol. 33, no. 12, pp. 2341–2353, Dec. 2011.
- [8] L. Xu, C. W. Lu, Y. Xu, and J. Jia, "Image smoothing via  $L_0$  gradient minimization," *ACM Trans. Graph.*, vol. 30, no. 6, Dec. 2011, Art. ID 174.
- [9] C. Tomasi and R. Manduchi, "Bilateral filtering for gray and color images," in *Proc. IEEE Int. Conf. Comput. Vis.*, Jan. 1998, pp. 836–846.
- [10] Z. Li, J. Zheng, Z. Zhu, S. Wu, and S. Rahardja, "A bilateral filter in gradient domain," in *Proc. Int. Conf. Acoust., Speech Signal Process.*, Mar. 2012, pp. 1113–1116.
- [11] P. Choudhury and J. Tumblin, "The trilateral filter for high contrast images and meshes," in *Proc. Eurograph. Symp. Rendering*, pp. 186–196, 2003.
- [12] F. Durand and J. Dorsey, "Fast bilateral filtering for the display of high-dynamic-range images," *ACM Trans. Graph.*, vol. 21, no. 3, pp. 257–266, Aug. 2002.
- [13] J. Chen, S. Paris, and F. Durand, "Real-time edge-aware image processing with the bilateral grid," *ACM Trans. Graph.*, vol. 26, no. 3, pp. 103–111, Aug. 2007.
- [14] K. He, J. Sun, and X. Tang, "Guided image filtering," *IEEE Trans. Pattern Anal. Mach. Intell.*, vol. 35, no. 6, pp. 1397–1409, Jun. 2013.
- [15] B. Y. Zhang and J. P. Allebach, "Adaptive bilateral filter for sharpness enhancement and noise removal," *IEEE Trans. Image Process.*, vol. 17, no. 5, pp. 664–678, May 2008.
- [16] Z. Li, J. Zheng, Z. Zhu, S. Wu, W. Yao, and S. Rahardja, "Content adaptive bilateral filtering," in *Proc. IEEE Int. Conf. Multimedia Expo*, Jul. 2013, pp. 1–6.
- [17] L. Itti, C. Koch, and E. Niebur, "A model of saliency-based visual attention for rapid scene analysis," *IEEE Trans. Pattern Anal. Mach. Intell.*, vol. 20, no. 11, pp. 1254–1259, Nov. 1998.
- [18] C. C. Pham, S. V. U. Ha, and J. W. Jeon, "Adaptive guided image filtering for sharpness enhancement and noise reduction," in *Advances in Image and Video Technology*. Berlin, Germany: Springer-Verlag, 2012.
- [19] G. Petschnigg, M. Agrawala, H. Hoppe, R. Szeliski, M. Cohen, and K. Toyama, "Digital photography with flash and no-flash image pairs," *ACM Trans. Graph.*, vol. 22, no. 3, pp. 664–672, Aug. 2004.
- [20] E. Eisemann and F. Durand, "Flash photography enhancement via intrinsic relighting," *ACM Trans. Graph.*, vol. 22, no. 3, pp. 673–678, Aug. 2004.
- [21] A. Zomet and S. Peleg, "Multi-sensor super-resolution," in *Proc. 6th IEEE Workshop Appl. Comput. Vis.*, Dec. 2002, pp. 27–31.
- [22] A. Torralba and W. T. Freeman, "Properties and applications of shape recipes," in *Proc. IEEE Comput. Vis. Pattern Recognit.*, Jun. 2003, pp. 383–390.
- [23] A. Levin, D. Lischinski, and Y. Weiss, "A closed-form solution to natural image matting," *IEEE Trans. Pattern Anal. Mach. Intell.*, vol. 30, no. 2, pp. 228–242, Feb. 2008.
- [24] R. C. Gonzalez and R. E. Woods, *Digital Image Processing*. Upper Saddle River, NJ, USA: Prentice-Hall, 2002.
- [25] A. K. Moorthy and A. C. Bovik, "A two-step framework for constructing blind image quality indices," *IEEE Signal Process. Lett.*, vol. 17, no. 5, pp. 513–516, May 2010.
- [26] S. G. Narasimhan and S. K. Nayar, "Chromatic framework for vision in bad weather," in *Proc. IEEE Conf. Comput. Vis. Pattern Recognit. (CVPR)*, Jun. 2000, pp. 598–605.
- [27] R. T. Tan, "Visibility in bad weather from a single image," in *Proc. IEEE Conf. Comput. Vis. Pattern Recognit. (CVPR)*, Jun. 2008, pp. 1–8.
- [28] X. Lv, W. Chen, and I.-F. Shen, "Real-time dehazing for image and video," in *Proc. 18th Pacific Conf. Comput. Graph. Appl.*, Sep. 2010, pp. 62–69.
- [29] J. Pang, O. C. Au, and Z. Guo, "Improved single image dehazing using guided filter," in *Proc. APSIPA ASC*, Xi'an, China, 2011, pp. 1–4.
- [30] M. van Herk, "A fast algorithm for local minimum and maximum filters on rectangular and octagonal kernels," *Pattern Recognit. Lett.*, vol. 13, no. 7, pp. 517–521, Jul. 1992.
- [31] E. B. Goldstein, *Sensation and Perception*. Wadsworth, OH, USA: Cengage Learning, 1980.
- [32] A. J. Preetham, P. Shirley, and B. Smits, "A practical analytic model for daylight," in *Proc. SIGGRAPH*, 1999, pp. 91–100.
- [33] R. Fattal, "Single image dehazing," in *Proc. SIGGRAPH*, 2008, pp. 1–9.

- [34] J. Kopf *et al.*, "Deep photo: Model-based photograph enhancement and viewing," in *Proc. SIGGRAPH Asia*, 2008, pp. 1–10.
- [35] T. Mertens, J. Kautz, and F. Van Reeth, "Exposure fusion: A simple and practical alternative to high dynamic range photography," *Comput. Graph. Forum*, vol. 28, no. 1, pp. 161–171, 2009.
- [36] Z. Li, J. Zheng, Z. Zhu, and S. Wu, "Selectively detail-enhanced fusion of differently exposed images with moving objects," *IEEE Trans. Image Process.*, vol. 23, no. 10, pp. 4372–4382, Oct. 2014.
- [37] P. Perona and J. Malik, "Scale-space and edge detection using anisotropic diffusion," *IEEE Trans. Pattern Anal. Mach. Intell.*, vol. 12, no. 7, pp. 629–639, Jul. 1990.



**Zhengguo Li** (SM'03) received the B.Sc. and M.Eng. degrees from Northeastern University, Shenyang, China, in 1992 and 1995, respectively, and the Ph.D. degree from Nanyang Technological University, Singapore, in 2001.

His current research interests include high dynamic range imaging, video processing, QoS, hybrid systems, and chaotic secure communication. He has co-authored one monograph, over 160 journal/conference papers, and holds six granted patents, including normative technologies on scalable extension of H.264/AVC. He has been actively involved in the development of H.264/AVC and HEVC since 2002. He had three informative proposals adopted by the H.264/AVC and three normative proposals adopted by the HEVC. He is currently with the Institute for Infocomm Research, Agency for Science, Technology and Research, Singapore. He is also an elected Technical Committee of the IEEE Visual Signal Processing and Communication. He served as the Technical Chair of the IEEE Conference on Industrial Electronics and Applications (ICIEA) in 2010, General Chair of the IEEE ICIEA in 2011, Technical Brief Co-Chair of SIGGRAPH Asia in 2012, the General Co-Chair of the Chinese Control and Decision Conference in 2013, and Workshop Chair of the IEEE International Conference on Multimedia and Expo in 2013. He has been an Associate Editor of the IEEE SIGNAL PROCESSING LETTERS since 2014. He was an Invited Lecturer by the 2011 IEEE Signal Processing Summer School on 3D and High Definition/High Contrast Video Processing Systems and a Distinguished Invited Lecturer by the IEEE International Conference on Industrial Informatics in 2012.



**Jinghong Zheng** (S'02–M'09) was born in China in 1977. She received the B.Sc. degree in electronic engineering from the Beijing Institute of Technology, Beijing, China, in 2000, and the Ph.D. degree in electronic and electrical engineering from Nanyang Technological University, Singapore, in 2006.

She has been with the Department of Signal Processing, Institute for Infocomm Research, Agency for Science, Technology and Research, Singapore, as a Scientist, since 2006. Her research interests include high dynamic range image processing, image fusion and enhancement, inpainting, error concealment/resilience of H.264 video, region of interesting video coding, scalable video coding, and video streaming.



**Zijian Zhu** was born in China in 1981. He received the B.E. degree from the Department of Computer Science and Engineering, Shanghai Jiao Tong University, Shanghai, China, in 2001, the M.Comp. degree from the National University of Singapore, Singapore, in 2007, and the Ph.D. degree in computer science from the University of Eastern Finland, Joensuu, Finland, in 2013. He joined the Institute for Infocomm Research, Agency for Science, Technology and Research, Singapore, in 2002, as a Research Officer. His current research interests include high dynamic range imaging/video, image noise reduction, and image enhancement. He was a recipient of the Tan Kah Kee Young Inventors' Silver Award in 2010, and the Nokia Scholarship in 2011.



**Wei Yao** (S'07–M'13) received the B.Eng. and Ph.D. degrees in electrical and electronic engineering from Nanyang Technological University (NTU), Singapore, in 2004 and 2013, respectively.

She has been with the Institute for Infocomm Research, Agency for Science, Technology, and Research, Singapore, as a Research Engineer, since 2004. Her research interests include digital video compression and transmission, and high dynamic range image compression and processing.



**Shiqian Wu** (M'02–SM'05) received the B.Eng. and M.Eng. degrees from the Huazhong University of Science and Technology (HUST), Wuhan, China, in 1985 and 1988, respectively, and the Ph.D. degree from Nanyang Technological University, Singapore, in 2001.

He is currently a Professor with the College of Machinery and Automation, Wuhan University of Science and Technology, Wuhan. He was an Assistant Professor, a Lecturer, and an Associate Professor at HUST, from 1988 to 1997. From 2000 to 2014, he was a Research Fellow or Research Scientist with the Agency for Science, Technology and Research, Singapore. He has co-authored the book entitled *Dynamic Fuzzy Neural Networks* (Singapore: McGraw-Hill, 2003). He has authored or co-authored over 100 scientific publications (book chapters and journal/conference papers). His current research interests include image processing, pattern recognition, machine vision, fuzzy systems, and neural networks.